Journal of Materials Science manuscript No.
(will be inserted by the editor)

Thin film nanoporous electrodes for the selective catalysis of oxygen in abiotically catalyzed micro glucose fuel cells

Uyen P. Do[1,*] · **Frode Seland**[2] · **Michel M. Maharbiz**[3] · **Kaiying Wang**[1] · **Øivind Johannesen**[1] · **Erik A. Johannessen**[1]

Received: date / Accepted: date

Abstract Selective reduction of oxygen is an important property of fuel cells designed to operate in a mixed fuel environment containing both oxidizing and reducing reactants. This would be of particular importance in the design of a long lasting energy supply unit powering implantable microsystems and running from exogeneous chemicals that is abundant in the body (such as glucose and oxygen). This paper presents the development of a nanoporous electrode for oxygen reduction in the presence of glucose. The electrode was fabricated by e-beam deposition of palladium thin films on porous ceramic aluminium oxide (AAO) substrates with a pore size of 100 and 200 nm respectively. The porous nature of the electrodes improved the catalytic properties by increasing the real surface area close to 100 times the geometric surface area. At a dissolved physiological oxygen (DO) concentration of 2 ppm, the maximum exchange current density was found to be $2.9\times10^{-3} \pm 0.5\times10^{-3}$ μA cm^{-2} whereas the potential reduction due to the addition of 5 mM glucose was about 20.6 ± 16.1 mV. The Tafel slopes were measured to be about 60 mV per decade. After running for 21 hours in a physiological saline solution with 2 ppm DO and 3 mM glucose, the reduction in the electrode operational potential was -0.13 mV h^{-1} under a load current density of 4.4 μA cm^{-2}. These results suggest that nanoporous AAO cathodes coated with palladium offers a reasonable catalytic performance with a good selectivity towards oxygen in the presence of glucose.

Keywords Abiotical catalyst · nanoporous cathode · palladium · glucose fuel cells

1 Introduction

The invention of the artificial pacemaker marked the dawn of implantable electronic devices that have now been successfully used in medicine for more than five decades [1]. Current applications extend to implantable neuroprosthetic devices [2] such as cochlear implants [3] and neural stimulating electrodes [4–6], as well as microfabricated devices targeting temperature, blood pressure, immuno-isolation, drug delivery, and microinjection [7,8]. Still, one critical issue has remained with respect to the power supply since stringent size constraints of the implant have compromised the available space required by batteries. These have often occupied more than half the volume of the implantable device [9] and consequently alternative means of power sources that may offer higher energy densities or lifetimes have been considered. Energy harvesters based on vibration [10,11], thermal gradients [12,13] and exogeneous chemicals [14,15] have therefore emerged as the most promising candidates. In this respect, the use of glucose and dissolved oxygen (DO) may hold the best promise of a long term energy supply for electronic implants due to their relative abundance in all tissues and their limited-dependency to ambient factors.

[1] Department of Micro- and Nano Systems Technology, Faculty of Technology and Maritime Sciences, University College of Southeast Norway
Raveien 215, 3184 Borre, Norway

[2] Department of Materials Science and Engineering, Faculty of Natural Sciences and Technology, Norwegian University of Science and Technology, NTNU
7491 Trondheim, Norway

[3] Berkeley Sensor and Actuator Center, University of California at Berkeley
403 Cory Hall,CA 94720-1774, USA

* Corresponding author: Uyen P. Do, Tel.: +47 3100 9365, E-mail: Uyen.Do@hbv.no

The process of harvesting glucose for electrical energy conversion has been performed by different classes of glucose fuel cells depending on the type of catalyst used. Microbial fuel cells utilize whole living microorganisms such as yeast and bacteria to fully oxidize glucose to its end products CO_2 and water [16]. Enzymatic fuel cells utilise isolated enzymes, such as glucose oxidase or hexokinase that are directly immobilised on the electrode surfaces [17–19]. In contrast, abiotically catalysed fuel cells bypass the use of a biological agent in favour of a direct catalysis by non-biological materials such as noble metals (and their alloys) or activated carbon [20,21]. Although non-enzyme catalysed oxidation of glucose results in lower power densities compared to the use of enzymes (as well as lower conversion efficiencies compared to the use of microbes), they benefit from extended operational lifetimes and higher stability by not relying on biological agents that degrades with time.

A conventional fuel cell operates by feeding reactants through separate channels to each side of an electrolyte, where the anode and cathode is spatially separated by the electrolyte. However, a micro glucose fuel cell will operate where both reactants (i.e. glucose and oxygen) are present in the same fluid. Obtaining an adequate efficiency of the fuel cell acquires the use of both a glucose selective anode as well as an oxygen selective cathode. Considering the latter, common catalyst material such as platinum (Pt) or Raney-Pt alloy offers both good catalytic properties towards DO reduction and glucose oxidation [20,22,23], and is therefore not a perfect material if both analytes are present. Activated carbon may represent an alternative but has a lower overall catalytic activity compared to the Raney-Pt alloy in the presence of glucose [24,25]. Other catalysts such as silver, gold, ferric phthalocyanine have drawbacks of either low catalytic activity towards DO reduction or a high catalytic activity towards glucose oxidation [20]. In contrast, palladium (Pd) possesses some of the same qualities as Pt and is currently used in catalytic converters, fuel cells and hydrogen sensors [26]. Its selective properties towards oxygen reduction have already been explored in acid and alkaline media [20,27,28], where the Pd catalyst was deposited by sputtering, by chemical synthesis or by electrodeposition [27–29]. However, the properties towards oxygen reduction of evaporated Pd thin films in neutral physiological solutions (pH = 7.4) has yet to be investigated in detail, especially in the presence of glucose.

The real surface area of the electrode system (in contrast to the geometric surface area) represents another challenge since it governs the degree of size reductions possible without compromising the power generating capacity of the fuel cell. Some methods based on the use of Raney-alloy catalyst or coating of electrodes with carbon nanotubes or carbon paper as a porous catalyst support have been investigated to increase the real surface area [21,24]. In contrast, porous alumina or anodized aluminium oxide (AAO) possesses several favorable characteristics as a catalyst support due to its large real surface area, tunable and uniform pore diameter, high pore density, and good thermal stability [30,31]. AAO membranes have also previously been used in enzymatic glucose fuel cell applications [32], and are considered to be a potent candidate for use in micro abiotic glucose fuel cells due to its commercial availability, small size and adaptability towards microfabrication technologies.

This paper explores the potential benefit of applying porous AAO membranes as an electrode substrate for a thin film Pd catalyst. The catalyst / membrane assembly forms a nanoporous electrode which was characterized for its oxygen selective properties under simulated physiological conditions with different oxygen concentrations both in the presence and absence of glucose. The Pd nanoporous electrode was also characterized electrochemically in order to investigate the real surface area and the oxygen reduction activity.

2 Materials and Methods

2.1 Fabrication

Nanoporous AAO membranes with a diameter of 13 mm, a thickness of 60 μm and a pore diameter of 100 and 200 nm were used as electrode substrates (Anodisc 6809-7013 and 6809-7023, Fisher Scientific, UK). The catalyst was deposited by e-beam evaporation of Pd (EVMPD35SHOT, Kurt J. Lesker, US) to form thin metal films with a thickness of 200 nm. The different pore diameters were chosen to investigate the relationship between the surface topography and catalytic ability of the electrode. The substrates were assembled in a custom-made holder taking 10 membranes in one batch. The substrates were rotated at an angle during the evaporation process in order to achieve better material coverage inside the vertical walls of the pores. Surface analysis were done both prior and after Pd deposition by a scanning electron microscope (SEM, LEO 1550, ZEISS, Germany). Analysis of the material composition were done both prior and after Pd deposition by the EDS function of an SEM (Philips XL30, The Netherlands). The samples were diced into smaller pieces and attached to a standard $1\times3''$ glass slide by silicone rubber (3140 RTV Coating, Dow Corning, US)

and copper wires were bonded using silver epoxy (EPO-TEK EE129-4, Epoxy Technology, Inc., US) to form an electrical connection. Additional silicone was then applied to electrically insulate the copper wire bond so that only the Pd catalyst is exposed to the aqueous test solution.

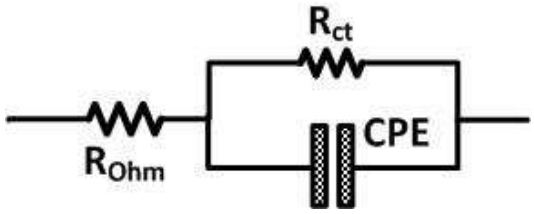

Fig. 1 Electrical equivalent circuit of the Pd electrodes.

2.2 Surface area determination

Since Pd is a hydrogen absorbing metal, the real surface area cannot be evaluated from conventional hydrogen adsorption-desorption studies [33]. Instead, the charge obtained from the oxide growth and reduction peak with the electrode immersed in 0.5 M H_2SO_4 could be used as an estimation of the real surface area [34]. The H_2SO_4 solution was prepared freshly and deaerated with nitrogen gas. A Pt wire of 0.5 mm diameter, and 6 cm length (P/3640/89, Fisher Scientific Limited, UK) was coiled up and used as the counter electrode. All potentials mentioned in this paper were referred to a standard Ag|AgCl reference electrode in 4 M saturated KCl (Thermo Scientific, USA). Cyclic voltammograms (CVs) of the electrode samples were obtained in the potential region of 0 V to 1.2 V at a scan rate of 50 mV s^{-1} using a potentiostat (Versastat 3, Princeton Instruments, US). Considering that all oxide reduction is done from around 0.2 V [34], the reduction charge of the palladium oxide (PdO) is calculated in the potential region of 0.2 - 1.2 V. Since the charge density associated with the reduction of one monolayer of PdO is considered to be 424 μC cm^{-2} [34], the real surface area of the Pd samples can be obtained by dividing with this charge density.

This real surface area of the Pd electrodes was confirmed by conducting a measurement of the double layer capacitance at the electrode-electrolyte interface. These experiments were preformed in a deaerated solution of 0.5 M H_2SO_4 and electrochemical impedance spectroscopy (EIS) were performed over a frequency range from 10 mHz to 10 kHz using the EIS function of a Zahner electrochemical workstation (IM6, Zahner-elektrik GmbH, Germany). The potentiostat mode function at a constant potential of 0.3 V with an AC amplitude of 5 mV was used. The electrical equivalent model used to describe the electrode characteristics is presented in Fig. 1. The SIM function of the Zahner electrochemical workstation was used to estimate the parameters of the charge transfer resistance (R_{ct}), the ohmic resistance (R_{ohm}) and the constant phase element (*CPE*) including the constant representative (Q) and the exponent (m). The double layer capacitance C_{dl} is then extracted from the *CPE* parameters by the following equation [35]:

$$C_{dl} = \left[Q \left(\frac{R_{ohm} R_{ct}}{R_{ohm} + R_{ct}} \right)^{1-m} \right]^{1/m} \tag{1}$$

A *CPE* was considered to be a better model for the double layer capacitance compared to an ideal capacitor, since it satisfied the F- ratio test for a parameter addition to the equivalent circuit [36]. The F- ratio can be estimated by the following formula [36]:

$$F\left(a, 2N-k\right) = \frac{\left[\chi^2\left(k-1\right) - \chi^2\left(k\right)\right]\left(2N-k\right)}{a\chi^2\left(k\right)} \tag{2}$$

where a is the number of the additional parameters, ($2N$-k) is the degrees of freedom, N is the number of data points, k is the number of parameters in the new circuit and χ^2 is the goodness-of-fit for the parameters. Here we have $a = 1$, $k = 4$, $N = 128$, $\chi^2(3)$ and $\chi^2(4)$ for the equivalent circuit with the ideal capacitor and the *CPE*, respectively, in order to find F values of 420 for the 100 nm pore and 1092 for the 200 nm pore electrodes. Those F values have probabilities of being exceeded by chance of much less than 1% which is considered as acceptable.

Since the double layer capacitance of an ideally smooth Pd surface at 0.3 V is estimated to be 24.5 μC cm^{-2} [37], the real surface area of the Pd electrode can be found by dividing the recorded value of the double layer capacitance with this area specific double layer capacitance.

2.3 Electrode performance

The thermodynamic predicted voltage output (E_{rev}) for the oxygen reduction reaction $O_2 + 2H_2O + 4e^- \rightarrow 4OH^-$ would be equivalent to 0.546 and 0.550 V considering the electrode immersed in phosphate buffered saline, PBS (pH = 7.4), at 25^{o}C with a concentration of 1 and 2 ppm DO, respectively. The electrode potential is then found according to [38] in which the thermodynamical predicted voltage output is subtracted by different potential losses:

$$E = E_{rev} - \eta_{act} - \eta_{ohmic} - \eta_{con} \tag{3}$$

where η_{act} is the activation overpotential (initiating the charge transfer reaction), η_{ohm} is the ohmic overpotential (due to the area specific resistance of the electrode) and η_{con} is the concentration overpotential (if the concentration of reactants on the electrode surface is lower than in the bulk). At low current densities, one can assume that the transport of reactants will keep pace with the charge transfer reaction resulting in $\eta_{\text{con}} \Rightarrow 0$. In contrast, the ohmic overpotential still needs to be considered:

$$\eta_{ohmic} = j \times ASR_{ohm} \tag{4}$$

where j is the cathodic current density (A cm^{-2}) and ASR_{ohm} is the area specific resistance (Ωcm^2). Both units are referred to the geometric surface area. Rearranging for η_{act} yields:

$$\eta_{act} = E_{rev} - E - \eta_{ohm} \tag{5}$$

Equation (4) and (5) can be applied to calculate η_{ohmic} and η_{act} based on two selected data points (A and B) obtained from the electrode polarization curves in Fig. 5. From this, the exchange current density can be estimated by considering the Tafel equation:

$$\eta_{act} = \frac{RT}{\alpha nF} \times ln\ \frac{j}{j_0} \tag{6}$$

where R is the universal gas constant (8.314 JK^{-1} mol^{-1}), T is the absolute temperature (K), α is the transfer coefficient, n is the number of transferred electrons, F is Faradays constant (96485 Cmol^{-1}), j is the cathodic current density (A cm^{-2}) and j_0 is the exchange current density (A cm^{-2}). Assuming no other reaction occuring, j_0 can be estimated by combining the Tafel expressions at point A and B:

$$j_0 = exp(\frac{\eta_{act_A} \times lnj_B - \eta_{act_B} \times lnj_A}{\eta_{act_A} - \eta_{act_B}}) \tag{7}$$

where η_{actA} and η_{actB} are the activation overpotentials at point A and B on the polarisation curve respectively, whereas j_{A} and j_{B} are the corresponding cathodic current densities. The Tafel slopes between point A and B were estimated through the Tafel plot of IR-corrected potentials ($E_{\text{cor}} = E + \eta_{\text{ohmic}}$) vs $\log_{10} j$.

The experimental protocol was based on the one described by Kerzenmacher et al. [24]. The test solution consisted of 500 mL PBS (P3813, Sigma-Aldrich, US) diluted to a concentration of 10 mM at pH = 7.4. All experiments were conducted at room temperature (25^{o}C). Glucose (G7525, Sigma-Aldrich, US) was added to a concentration of 3 and 5 mM to simulate the variation in physiological levels of the interstitial fluid in human tissue [20]. The addition of DO was controlled by mixing corresponding amounts of air and nitrogen gas that was pumped into the test vessel. The level was continuously monitored by a DO meter (C3040, Consort, Belgium), and the DO concentrations were also selected to correspond to a physiological range in human tissues ranging from 0.03 mM ≅ 1 ppm ≅ 3.5 % to 0.06 mM ≅ 2 ppm ≅ 7 %. A DO level of 2 ppm is approximately the value found in the subcutaneous tissue of the human arm (a proposed location of the fuel cell) and was thus considered as the maximum value [24]. The minimum value of 1 ppm was chosen as the oxygen tension in active respiratory tissue with the femoral muscle of the mouse acting as a model [24]. Stable values was obtained by applying a current step of 1.1 μA cm^{-2} for 1 and 2 ppm DO to increase the load current density for a period of 2 hours from an initial open circuit potential (OCP).

2.4 Electrochemical impedance spectroscopy

Similar to section 2.2, the EIS analysis was performed over a frequency range from 10 mHz to 10 kHz. The galvanostat mode function at a constant current density with an AC amplitude of 5 nA was used throughout the EIS measurement. The measurement conditions were similar to that described in section 2.3. The electrical equivalent circuit in Fig. 1 and the SIM function were used to estimate R_{ct}, ASR_{Ohm} and the *CPE*. The double layer capacitance, from equation (1), was modeled as a *CPE* as justified by the F-ratio test of adding an additional parameter in equation (2).

3 Results and discussion

3.1 Electrode structure

The native surface topography of the AAO substrates with 100 and 200 nm pores is shown in Fig. 2.a-b whereas the electrodes with evaporated Pd film deposits on the interpore region of AAO surface is shown Fig. 2.c-d. This behavior is similar to that observed from sputtered Pt atoms on porous AAO substrates reported in [39]. The cluster formation of Pd particles on the AAO surface shows that the process of material deposition by e-beam evaporation includes two main steps: (i) initial atom stacking and (ii) subsequent cluster formation which grows in size and forms a homogeneous layer. It was further observed that the rims covered by the Pd became thicker with increasing thickness of the metal film. This resulted in geometrical shrinkages for both the 100 and 200 nm pores whereas the rims got thicker,

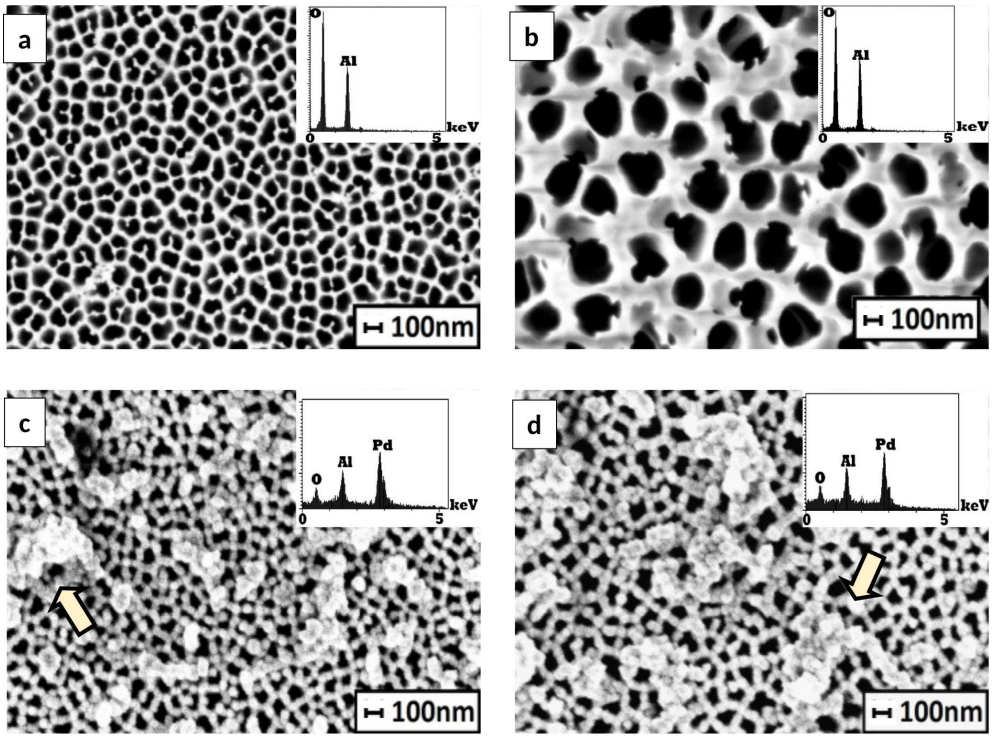

Fig. 2 Surface SEM images of the porous AAO substrates with (a) 100 nm and (b) 200 nm pores prior to Pd deposition. The surface topography changes for the electrodes equipped with (c) 100 nm and (d) 200 nm pores following the deposition of a 200 nm thick layer of Pd on top of the AAO substrates with the Pd clusters (arrows). Inserts show EDS measurements of the electrode surface.

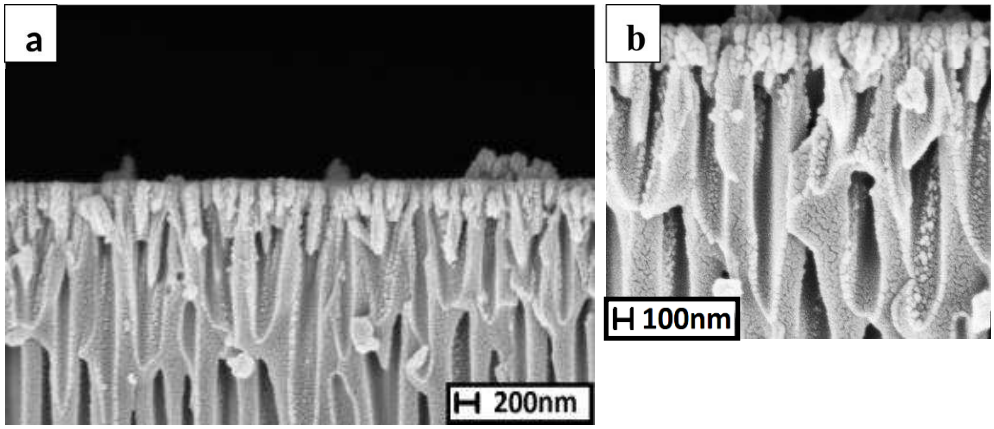

Fig. 3 (a) shows a typical cross-sectional SEM image of the porous AAO substrates coated with a 200 nm thick Pd film. (b) shows the formation of Pd clusters along the pore wall at a higher magnification of the SEM image.

and resulted in an overall increase in the real surface area.

The cross sectional images of the fabricated Pd cathode are shown in Fig. 3. The Pd clusters occur not only on the interpore region of the AAO surface but also around the rim of the pores and along the upper portion of the pore walls. The growth of Pd cluster around the pore rim could be a result of a surface effect [40]. In these cases, free surfaces such as edges or defects, are regions that harbour a high surface energy that act as seeding points for heterogeneous material nucleation [30]. The appearance of Pd clusters along the pore walls could be the result of deposition inside the vertical walls of the pores due to the sample rotating at an angle during the evaporation phase combined with the transport or diffusion properties of Pd atoms.

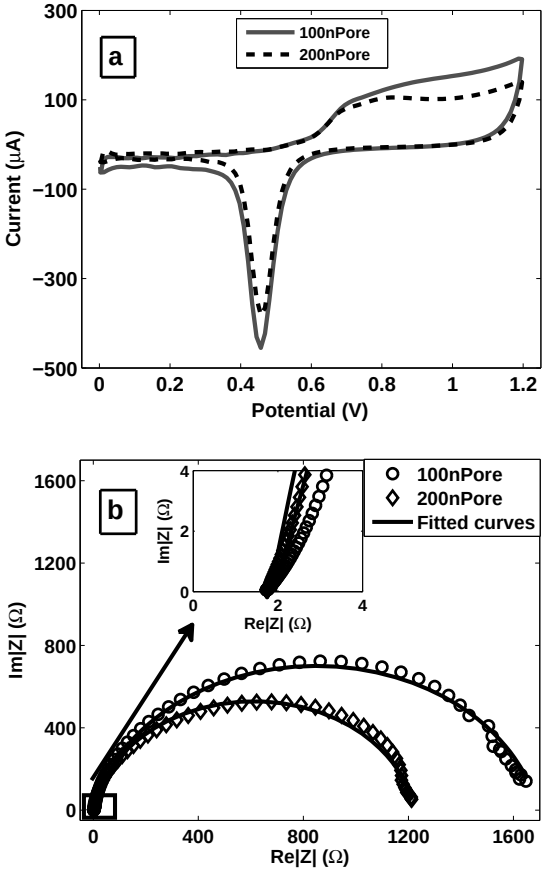

Fig. 4 (a) CV curves (a scan rate of 50 mV s^{-1}) and (b) EIS curves (at a potential of 0.3 V) of the Pd electrodes with a pore size of 100 and 200 nm, respectively. The experiments were conducted in 0.5 M H_2SO_4 vs saturated Ag|AgCl.

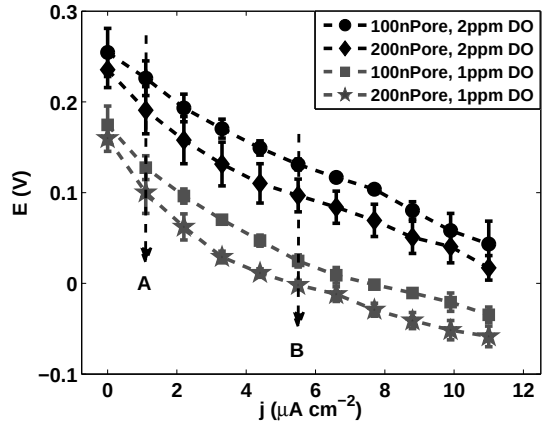

Fig. 5 Individual polarization curves of the Pd electrodes with pores of 100 and 200 nm at a concentration of 1 and 2 ppm DO vs saturated Ag|AgCl.

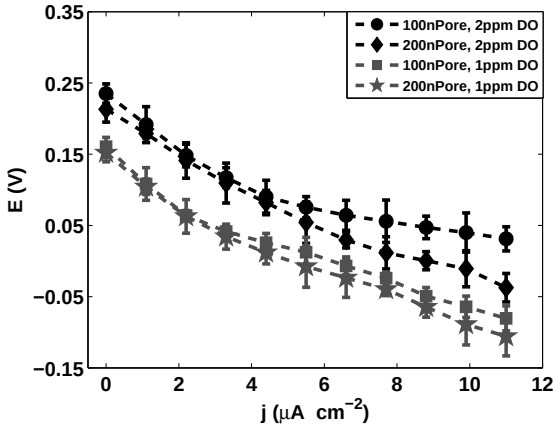

Fig. 6 Individual polarization curves of the Pd electrodes with 100 and 200 nm pores at a concentration of 1 and 2 ppm DO in PBS containing 5 mM glucose vs saturated Ag|AgCl.

3.2 Determination of the real surface area

The representative CVs and the EIS results of the thin film electrodes conducted in 0.5 M H_2SO_4 are shown in Fig. 4. The positive sweep (in Fig. 4.a) shows that the growth of oxides on the Pd surface results in the anodic currents starting near 0.55 V without a clear anodic peak. In the negative sweep (in Fig. 4.a), a sharp cathodic peak is formed around 0.46 V for both samples due to the reduction of the palladium oxide film. Based on the oxide reduction charge, the real surface area of the Pd electrodes with 100 and 200 nm pores were found to be 9.5 cm^2 and 7.8 cm^2, respectively.

The simple equivalent circuit (Fig. 1) fits well to the data of Pd electrodes (solid lines in Fig. 4b). Based on this curves, the double layer capacitance values were calculated to 245.8 ± 14.6 and 205.8 ± 12.3 μF for the electrodes with pores of 100 and 200 nm, respectively. This corresponds to a real surface area of 10 ± 0.6 cm^2 and 8.4 ± 0.5 cm^2, respectively. By using the same samples for both of the area determination experiments, the real surface area obtained from the double layer capacitance measurement are in good agreement with those received from the oxide reduction measurement. Comparing these values with the geometric area of the cathode samples (0.097 cm^2 and 0.101 cm^2, respectively), it is clear that the electrodes with the 100 nm pores have a larger real surface area (roughness factor f_r) than electrodes with 200 nm pores. This gives for the electrodes with 100 and 200 nm pores a roughness factor f_r of about 103 and 83, respectively.

3.3 Electrode performance

The relationship between the load current density (vs. geometric surface area) and the electrode potential for the nanoporous Pd electrodes with 100 and 200 nm diameter pores are presented in Fig. 5. The electrodes were investigated at two different DO concentrations

(1 and 2 ppm). Positive potentials are in accordance with the expected cathodic currents caused by the oxygen reduction at the working electrode. Fig. 5 shows that one generally obtain higher positive potentials (E) for the electrodes with 100 nm pores compared to the ones equipped with 200 nm pores in the whole current density range for each DO concentration. These results suggests that the Pd electrodes equipped with 100 nm pores gives a better performance in a simulated fuel cell mode than the ones with 200 nm pores. One also observes for all DO measurements that the potential differences between the Pd electrodes with 100 and 200 nm pores are slightly higher under a load condition than at zero current density (i.e. the average potential difference is approx. 17 ± 3 mV at zero load and approx. 31 ± 6 mV under load).

One may suggest the non-linear polarization curves at low current densities in Fig. 5 (i.e up to about 4.4 μA cm^{-2}) can be interpreted in terms of activation losses at the electrodes and one would therefore expect the activation potential loss to dominate the other loss mechanisms at low current densities. The variation of the current density vs. overpotentials can be described by a Butler-Volmer expression, or the equivalent Tafel expression (6):

$$j = j_0 \times exp\left(\frac{\alpha nF}{RT} \times \eta_{act}\right) \tag{8}$$

Consequently, in this region we disregard the overpotentials caused by the other loss mechanisms. This region is then used to construct Tafel curves and extract the exchange current densities (Fig. 9.a and b) as well as the Tafel slopes. Although linear Tafel curves are obtained, it is worth pointing out the narrow current range involved. This is a direct result of the small and limited current density observed in the polarization curves, being an invidious limitation to a reliable determination of the addiliated Tafel slope and exchange current density.

The observed differences in potentials for the electrodes with 100 and 200 nm pores at current densities below 4.4 μA cm^{-2} can be related to the differences in the so-called effective exchange current density j_0^* defined by the equation:

$$j_0^* = j_0 \times \frac{A_{real}}{A_{geo}} = j_0 \times f_r \tag{9}$$

where j_0 refers to the intrinsic exchange current density of a smooth plane surface, whereas the ratio $A_{\mathrm{real}}/A_{\mathrm{geo}}$, or the so-called roughness factor f_{r}, expresses the surface area enhancement of the real electrode area, A_{real}, compared to an ideally smooth, plane electrode area, A_{geo}.

As commented above, the real area of the 100 nm pore electrodes ($f_{\mathrm{r100}} = 103$) is slightly higher than the real electrode area of the 200 nm ones ($f_{\mathrm{r200}} = 83$). With reference to (9), the effective exchange current density of the 100 nm pore electrodes j_0^*(100nmPore) will be about 24% higher than the effective exchange current density of the 200 nm ones j_0^*(200nmPore). Hence, we may claim that the kinetic performance of the 100 nm pore electrodes would be better than the 200 nm pore ones as a result of an increased number of reaction sites or an increase in the reaction interface roughness, in other words.

An increase in the exchange current density can alternatively be visualized in a reduced activation overpotential, η_{act} in Eq. (6). Accordingly, we can suggest that the activation overpotential of the electrodes with 100 nm pores is lower than the overpotential of the 200 nm ones. Disregarding ohmic losses and concentration losses caused by mass transport, we may further suggest that the slightly higher observed potentials E of the electrodes with 100 nm pores when compared with the ones with 200 nm pores at the same DO concentration and at a given current density below 4.4 μA cm^{-2} is related to the reduced activation overpotential of the 100 nm pore electrodes.

The observed difference in the electrode potentials between the electrode with 100 and 200 nm pores can be compared to a Tafel-type expression. The expression has been developed from a modified Butler-Volmer expression which accounts for the roughness of the electrode surfaces. This gives:

$$\begin{aligned} \Delta E_{calc} &= \frac{2.303 \times RT}{\alpha nF} \times log_{10}\ \frac{j_{0,100}^*}{j_{0,200}^*} \\ &= S \times log_{10}\ \frac{j_{0,100} \times f_{r100}}{j_{0,200} \times f_{r200}} \end{aligned} \tag{10}$$

where $j_{0,100}$ and $j_{0,200}$ are the intrinsic exchange current density of the electrodes with 100 and 200 nm pores, respectively, f_{r100} and f_{r200} are the roughness factors of the same and S can be interpreted as the Tafel slope. We have assumed that the Tafel slope as well as the transfer coefficient, α, for the ORR are equal for both electrodes with 100 and 200 nm pores. Since the electrodes consist of Pd, we may also assume that the intrinsic exchange current densities are equal for both, i.e $j_{0,100} = j_{0,200}$. In this case, Eq. 10 will give an enhancement of, $\Delta E_{\mathrm{calc}} = 5.8$ mV, where we have applied the experimentally based value of $S = 61.8$ mV and the roughness factors of $f_{\mathrm{r100}} = 103$ and $f_{\mathrm{r200}} = 83$. The calculated value of $\Delta E_{\mathrm{calc}} = 5.8$ mV can be compared to the observed enhancement of $\Delta E = 31$ mV in the charge controlled region. It follows from Eq. 10 that the accuracy in the calculation of ΔE_{calc} is dependent on

the accuracy when determining the experimental value of the Tafel slope and the values of the real- and geometric surface areas. It is at present difficult to give a detailed consideration of the enhancement of the cell potential of the electrode with 100 nm pores compared to the one with 200 nm pores. One may tentatively suggest that an additional effect can be due to the improved catalytic surface condition at the electrode with 100 nm pores.

We have so far assumed that the intrinsic exchange current densities for the electrodes are equal due to the fact that they consist of the very same catalytic material, i.e. Pd. However, we can in a more complete consideration take into account that the intrinsic exchange current density is related to the properties of the actual catalytic site on the electrode surface. In this manner, the intrinsic current density can be related to e.g. the orientation of a specific crystal plane of the Pd particles, blocking of catalytic sites, the amount of adsorption, etc. Accordingly, we might assume that there can be a slight difference in the intrinsic exchange current densities for the electrodes with 100 and 200 nm pores. Hence, with reference to Eq. 10 we can obtain a calculated value of ΔE_{calc} in agreement with the observed enhancement ($\Delta E = 31$ mV) by assuming that the intrinsic exchange current density for the electrode with 100 nm pore is larger than the one with 200 nm pores by a factor of 2.6, i.e. $j_{0,100} = 2.6 \times j_{0,200}$. In this respect, the increased intrinsic exchange current density for the electrode with 100 nm pores reflects the improved catalytic surface condition when compared to the electrode with 200 nm pores.

It is further noted from simple Butler - Volmer kinetics that an increase in the DO concentration will result in an increase in the exchange current density. Thus, following the argumentation on the exchange current above, we should expect that the electrode potential of both electrodes at 2 ppm DO is higher than that at 1 ppm DO in the whole current density region.

The polarization curves at 5 mM glucose dissolved in PBS is presented in Fig. 6 as a function of different DO concentrations. The polarization curves shows a similar potential dependency vs the current density compared to the PBS solution without the added glucose. Again the potentials of the electrodes with 100 nm pores are slightly higher than the ones based on 200 nm pores. This result suggests that the oxygen reduction reaction performance of the electrodes with 100 nm pores is slightly better than for those with 200 nm pores, even at low DO concentrations in PBS with 5 mM glucose. As commented above, a higher electrode potential at a specific current density will result in a higher power density once implemented in a fuel cell mode.

The observed reduction in the potential (ΔE_{C}) of electrodes with 100 nm pores when 5 mM glucose was added into the PBS solution was approximately $\Delta E_{\mathrm{C}} = 26.7 \pm 11.8$ mV and $\Delta E_{\mathrm{C}} = 39.2 \pm 16.6$ mV at 1 and 2 ppm DO respectively. For the electrodes equipped with 200 nm pores, the potential reduction was measured to be approximately $\Delta E_{\mathrm{C}} = 37.4 \pm 17.1$ mV and $\Delta E_{\mathrm{C}} = 20.6 \pm 16.1$ mV at 1 and 2 ppm DO, respectively. It is difficult to give a univocal interpretation of the reduced Pd electrode potential caused by the presence of glucose. We may tentatively assume that the reduction of electrode potential is caused by adsorption of glucose as neutral molecules at the active electrode surface and thereby reduces the number of reaction sites. As commented above, this will reduce the effective exchange current density and consequently lower the electrode potential. It can be mentioned that the minor reduction of the Pd electrode potential caused by the presence of glucose is in agreement with well-known results from literature [41]. It has been reported that the morphology of the electrode surface will affect the adsorption characteristics of neutral organic molecules where the adsorption appears to be less on rough surfaces than on smooth, plane electrode surfaces. Compared to literature, the glucose sensitivity of Pd cathodes under load is rather low. The observed decrease in OCP at 1 ppm DO is about 14 mV for the electrodes with 100 nm pores and about 8 mV for the electrodes with 200 nm pores. These values are smaller than those reported for the Pt-Al cathode (measured without a Nafion diffusion barrier) under similar conditions [22].

A final study was performed with the electrodes immersed in a 5 mM glucose solution depleted for DO. According to [22], DO consumption at the outer region of the electrode could trigger oxygen depletion in the pores where the local potential is dominated by the presence of glucose. This effect would be dependent on the electrode geometry and the substrate with 200 nm pores could be more susceptible if the catalytic active material (Pd) had penetrated deep into the pores during fabrication. It was found that the OCP of the electrodes with 100 nm pores (-247.7 ± 9.5 mV) was approximately 23.3 mV lower than the OCP of the electrodes with 200 nm pores (-224.4 ± 5.7 mV). This result suggests that the electrodes with 100 nm pores may have an increased catalytic activity and that oxygen depletion will not be a dominating parameter for the electrodes with 200 nm pores under these measurement conditions. However, one should not over-interpret such small changes when based on OCP measurement alone.

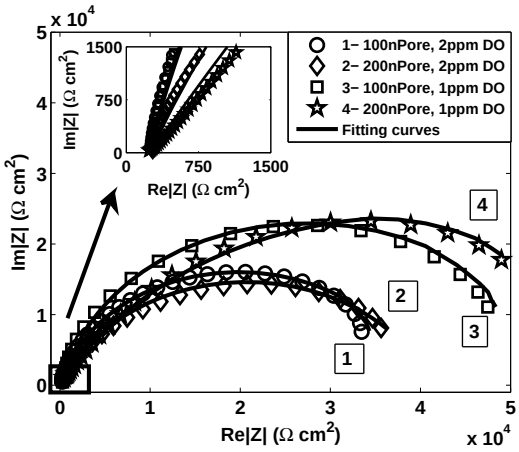

Fig. 7 Nyquist plot obtained on the Pd electrodes with 100 and 200 nm pores at different DO concentration of 1 and 2 ppm at a load current density of 3.3 μA cm^{-2} in PBS.

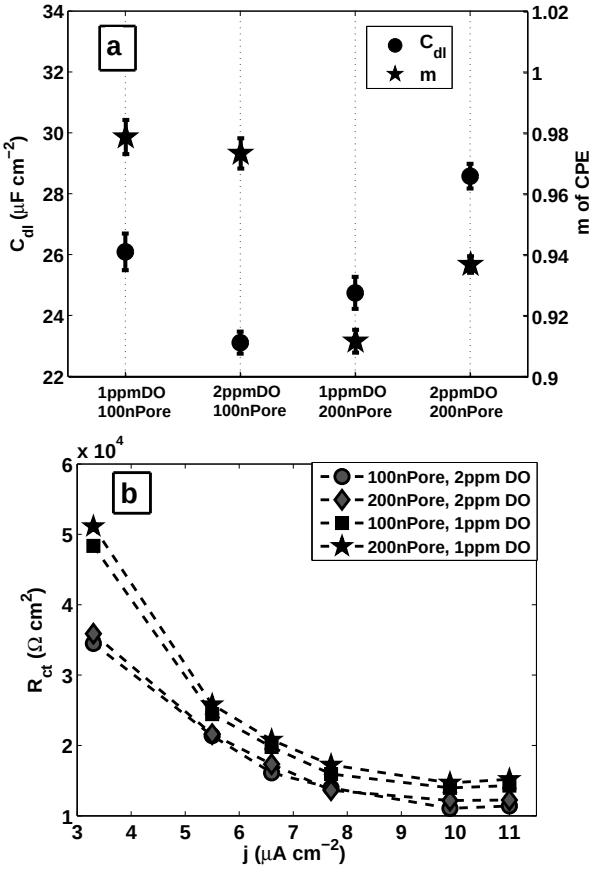

Fig. 8 (a) The double layer capacitance C_{dl} and coefficient m of *CPE* recorded in PBS; (b) The R_{ct} of the Pd electrodes was obtained at different current densities by using the simple circuit in (Fig. 1), at DO concentrations of 1 and 2 ppm in PBS.

3.4 Electrochemical impedance spectroscopy study

The plots of the electrodes at a load current density of 3.3 μA cm^{-2} (vs. geometric surface area), presented in Fig. 7, are typical Nyquist plots of the Pd electrodes at an oxygen concentration of 1 and 2 ppm in PBS. The area specific Ohmic resistance $ASR_{\rm ohm}$ is 224.8 $\pm$ 13.2 Ωcm^2 and 249.9 $\pm$ 4.1 Ωcm^2 for the electrodes with 100 and 200 nm pores, respectively. This is a relative large value compared to classical macro-fuel cell electrodes based on, for example, carbon cloth [38] where the electrolyte resistance dominates. The measurement have been performed by a classical three electrode cell without applying a Luggin capillary. The exclusion of the Luggin capillary is related to the "high" conductivity value of the 10 mM PBS (σ= 1.5Ω^{-1}cm^{-1}) used as the electrolyte in this study. Alternative measurement with a 2 electrode setup (between a working electrode and a counter/reference electrode) gives comparable ASR values of the 100 and 200 nm pore electrodes (i.e. about 180 - 225 Ωcm^2) which further suggests that we can disregard the ohmic drop caused by the PBS electrolyte. It is at present difficult to give a univocal interpretation of the rather high ASR values of the electrodes. Hence, we may tentatively suggest that the high ASR values can be related to a passive film formation on the electrode surface (e.g. PdOx) during the oxygen reduction, resulting in higher electronic resistances [42].

The observed slightly depressed semicircles can be interpreted by means of the equivalent circuit in Fig. 1, where the constant phase element, *CPE*, includes the deviation from ideal capacitance behavior. As shown in Fig. 8.a, this deviation was small with the coefficient m of the *CPE* corresponding to approximately m = 0.95 $\pm$ 2.20 $\times$ 10^{-3}. In all cases, the depressed semicircle "diameter" (i.e. the distance between the interception points on the real axes) depends on the oxygen concentration and the pore diameter. The dependence of the charge transfer resistance $R_{\rm ct}$ and the double layer capacitance $C_{\rm dl}$ on the oxygen concentration and the pore diameter is shown in Fig. 8. The values of R_{ct} have been obtained by extrapolating the Nyquist plots. There is not a clear correlation between $C_{\rm dl}$ or the coefficient m of the *CPE* with respect to the pore diameter or the DO concentration in PBS. However, the values of $C_{\rm dl}$ per unit area measured on the electrodes in a PBS solution (pH = 7.4) are comparable to the range found in both acid and alkaline media [27,28].

The $R_{\rm ct}$ will normally decrease with an increase in the load current density, or an increase in the overpotential. Since $R_{\rm ct}$ is mainly determined by the rate of the oxygen reduction process at the surface of the catalyst layer, the reduction of $R_{\rm ct}$ reflects the increasing driving force for the oxygen reduction reaction. It was also observed that for all the electrodes, the $R_{\rm ct}$ at 2

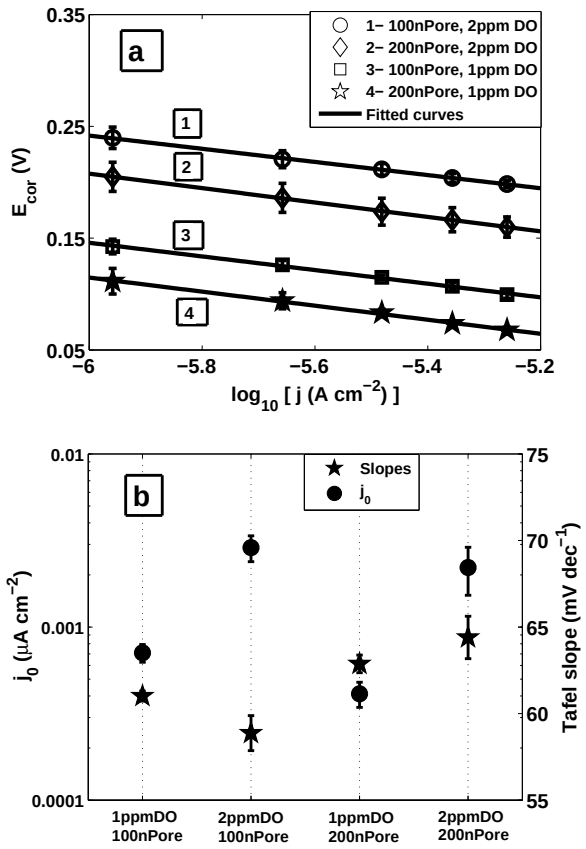

Fig. 9 (a) The Tafel plots and (b) the exchange current density and Tafel slope of the Pd electrodes at DO concentrations of 1 and 2 ppm in PBS solution vs saturated Ag|AgCl.

ppm DO is smaller than that at 1 ppm due to the higher reactant concentration supporting the oxygen reduction process.

The Tafel plots of IR corrected curves, the exchange current density j_0 and the Tafel slopes for the electrodes are presented in Fig. 9 at DO concentration of 1 and 2 ppm. In Fig. 9.a, the Tafel slopes were estimated from the slopes of the fitting curves to the EIS analysis performed at the overpotential range between point A (at 1.1 μA cm^{-2}) and point B (at 5.5 μA cm^{-2}) in Fig. 5. The Tafel slopes are found to be more or less independent on the pore diameter and the oxygen concentration with values around 60 mV dec^{-1}. This is in agreement with the Tafel slope reported by Sun et al. for the Pd catalyst supported on C [28].

The j_0 that was estimated from (7) and the fitting curves in Fig. 9.a gave the same values. It is known that the reaction kinetics increases with the increase of the reactant concentration at a constant current load. This will result in an increase of j_0 as demonstrated by the average calculated values of both samples (100 and 200 nm pore electrodes) obtained at 2 ppm DO ($2.5 \times 10^{-3} \pm 0.5 \times 10^{-3}$ μA cm^{-2}) compared to that of 1 ppm DO ($5.6 \times 10^{-4} \pm 0.5 \times 10^{-4}$ μA cm^{-2}). The best value for $j_0 = 2.9 \times 10^{-3} \pm 0.5 \times 10^{-3}$ μA cm^{-2} was recorded for the electrodes with 100 nm pores at a DO concentration of 2 ppm. The exchange current density of Pd films deposited by e-beam evaporation is generally similar to that obtained from sputtered Pd films [27].

3.5 Electrode stability

The results of chronopotentiometric experiments of electrodes immersed in PBS containing 3 mM glucose and 2 ppm DO at a load current density of 4.4 μA cm^{-2} (vs. geometric surface area) over a period of 24 hours, are presented in Fig. 10. The recording at t = 0 represents the OCP just prior to the onset of the measurement.

During the first hour, the electrode potentials reduced due to the effect of the applied load current. The potentials of the electrodes initially drop and stabilize to a value of approx. 70 - 80 mV after 4 hours. Although the potential drift rates of the electrodes with 100 and 200 nm pores was measured to be 1.57 mV h^{-1} and 1.45 mV h^{-1} respectively after the first hour, this decreased to 0.13 mV h^{-1} and 0.6 mV h^{-1} during the last 3 hours. This shows that the Pd catalyst stabilize under load with time compared to the Pt-Raney electrodes (0.9 mV h^{-1} for the electrodes without the diffusion barrier) [22]. The explanation for the reduction in electrode potential may result from the adsorption of reaction intermediates gradually deactivating the active surface. This causes a reduction in the effective j_0 and consequently decreasing in the electrode potentials. The electrodes with 100 nm pores exhibit a slightly higher positive potential (10 $\pm$ 3 mV) compared to the electrodes with 200 nm pores in accordance with earlier observations.

4 Conclusion

Electrodes functioning as nanoporous oxygen selective cathodes have been fabricated by depositing Pd thin films by e-beam evaporation on substrates made from AAO membranes. The morphologies of the surface and the cross section of the e-beam evaporated Pd film demonstrate that the pores shrink due to the accumulation of catalyst material on the rim as well as in the pore as evident by the formation of clusters on the inner walls of the AAO membranes. The larger real surface area of electrodes with 100 nm pores results in a higher exchange current density j_0, a lower charge transfer resistance R_{ct} and, consequently, a better oxygen reduction

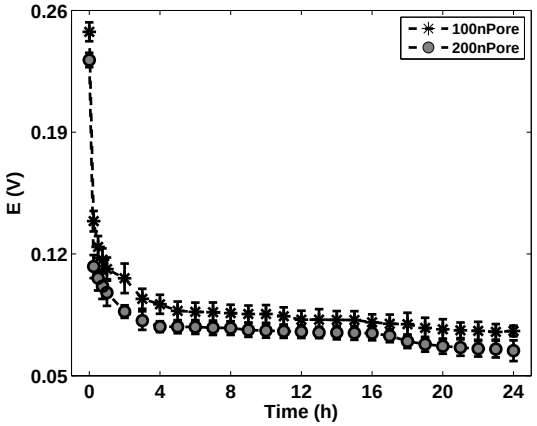

Fig. 10 Chronopotentiometric response of nanoporous Pd electrodes at a load current density of 4.4 μA cm^{-2}, at 2 ppm DO in PBS with 3 mM glucose vs saturated Ag|AgCl.

performance compared to the electrodes with 200 nm pores. The potential of tailoring the surface area and catalytic performance as a function of pore size demonstrates the advantages of using nanoporous AAO membranes with Pd as the catalyst in the design of oxygen selective electrodes in the presence of glucose. Future work will seek to combine this cathode with a glucose selective anode in a combined micro fuel cell system running on endogeneous fuel from the body.

Acknowledgements The authors would like to thank technical staff and colleagues at University College of Southeast Norway (HSN) and UC Berkeley for their assistance in this work. The work was supported by the Norwegian PhD Network on Nanotechnology for Microsystems, The Norwegian Centre for International Cooperation in Higher Education (SIU), The Ministry of Church and Education and The Research Council of Norway.

References

1. B. Larsson, H. Elmqvist, L. Ryden, H. Schuller, PACE **26**, 114 (2003)
2. V.S. Polikov, P.A. Tresco, W.M. Reichert, Journal of Neuroscience Methods **148**(1), 1 (2005)
3. G. Clark, L. Cohen, P. Busby. Implant device (2003)
4. R.e.a. Harrison, in *IEEE Intl. Symposium on Circuits and Systems (ISCAS 2008)* (2008)
5. K. Wise, D. Anderson, J. Hetke, D. Kipke, K. Najafi, Proceedings of the IEEE **92**(1), 76 (2004)
6. C. Thomas, Neurophysiol **84**(1), 591595 (2000)
7. A.C.R. Grayson, R.S. Shawgo, A.M. Johnson, N.T. Flynn, Y.W. Li, M.J. Cima, R. Langer, Proceedings of the IEEE **92**(1), 6 (2004)
8. E. Johannessen, O. Krushinitskaya, A. Sokolov, P. Hafliger, A. Hoogerwerf, C. Hinderling, K. Kautio, J. Lenkkeri, E. Esko Strommer, V. Kondratyev, T. Tannessen, T. Mollnes, H. Jakobsen, E. Zimmer, B. Akselsen, Journal of Diabetes Science and Technology **4**, 882 (2010)
9. V.S. Mallela, V. Ilankumaran, N. Rao, Indian Pacing and Electrophysiology Journal **4**(4), 201 (2004)
10. P.D. Mitcheson, E.M. Yeatman, G.K. Rao, A.S. Holmes, T.C. Green, Proceedings of the IEEE **96**(9), 1457 (2008)
11. S.P. Beeby, M.J. Tudor, N.M. White, Measurement Science and Technology **17**(12), R175 (2006)
12. Y. Yang, X.J. Wei, J. Liu, Journal of Physics D-Applied Physics **40**(18), 5790 (2007)
13. A. Lay-Ekuakille, G. Vendramin, A. Trotta, G. Mazzotta, in *Medical Measurements and Applications, 2009. MeMeA 2009. IEEE International Workshop on* (2009), pp. 1–4
14. M.E. Nielsen, C.E. Reimers, H.K. White, S. Sharma, P.R. Girguis, Energy & Environmental Science **1**(5), 584 (2008)
15. D.E. Holmes, D.R. Bond, R.A. ONeil, C.E. Reimers, L.R. Tender, D.R. Lovley, Microbial Ecology **48**(2), 178 (2004)
16. D.R. Lovley, Current Opinion in Biotechnology pp. 327–332 (2006)
17. A.E. Franks, K.P. Nevin, Energies **3**, 899 (2010)
18. H.Y. Wang, A. Bernarda, C.Y. Huang, D.J. Lee, J.S. Chang, Bioresource Technology **102**(1), 235 (2011)
19. I. Ivanov, T. Vidakovic-Koch, K. Sundmacher, Energies **3**(4), 803 (2010)
20. S. Kerzenmacher, J. Ducree, R. Zengerle, F.V. Stetten, Journal of Power Sources **182**, 1 (2008)
21. S. Kerzenmacher, U. Kraling, T. Metz, R. Zengerle, F. von Stetten, Journal of Power Sources **196**(3), 1264 (2011)
22. S. Kerzenmacher, U. Kraling, M. Schroeder, R. Bramer, R. Zengerle, F. von Stetten, Journal of Power Sources **195**(19), 6524 (2010)
23. A. Kloke, B. Biller, S. Kerzenmacher, U. Kraling, R. Zengerle, F.v. Stetten, in Proceeding of Eurosensors pp. 1416–1419 (2008)
24. S. Kerzenmacher, J. Ducree, R. Zengerle, F.v. Stetten, Journal of Power Sources **182**, 66 (2008)
25. S. Kerzenmacher, R. Sumbharaju, J. Ducre, R. Zengerle, F.v. Stetten, The 14th International Conference on Solid-State Sensors, Actuators and Microsystems pp. 125–128 (2007)
26. M. Johansson, L.G. Ekedahl, Applied Surface Science **173**(12), 122 (2001)
27. O. Savadogo, K. Lee, K. Oishi, S. Mitsushima, N. Kamiya, K.I. Ota, Electrochemistry Communications **6**(2), 105 (2004)
28. W. Sun, A. Hsu, R. Chen, Journal of Power Sources **196**(10), 4491 (2011)
29. K.M. Kost, D.E. Bartak, B. Kazee, T. Kuwana, Analytical Chemistry **62**(2), 151 (1990)
30. K.T. Huang, P.C. Kuo, Y.D. Yao, Thin Solid Films **517**(11), 3243 (2009)
31. S.H. Yoo, L. Liu, S. Park, Journal of Colloid and Interface Science **339**(1), 183 (2009)
32. T. Zhao, *Micro Fuel Cells - Principles and Applications* (Elsevier Inc., San Diego, California 92101-4495, USA, 2009)
33. S. Trasatti, O.A. Petrii, Pure & Appl. Chem. **63**(5), 711 (1991)
34. M. Grden, M. Lukaszewski, G. Jerkiewicz, A. Czerwinski, Electrochimica Acta **53**(26), 7583 (2008)
35. F. Seland, R. Tunold, D.A. Harrington, Electrochimica Acta **51**(18), 3827 (2006)
36. P.R. Bevington, D.K. Robinson, *Data Reducion and Error Analysis for the Physical Sciences*, 3rd edn. (McGraw Hill, New York, 1969)

37. B. Losiewicz, L. Birry, A. Lasia, Journal of Electroanalytical Chemistry **611**(12), 26 (2007)
38. R. O'Hayre, S.W. Cha, W. Colella, F.B. Prinz, *Fuel Cell FFundamental - 2nd ed.* (John Wiley & Sons, Inc., Hoboken, New Jersey, 2009)
39. S. Wu, P. Brault, C. Wang, Journal of Optoelectronics and Advanced Materials **12**, 451 (2010)
40. Z. Huajun, Z. Jinhuan, G. Zhenghai, W. Wei, Journal of Magnetism and Magnetic Materials **320**(34), 565 (2008)
41. S. Srinivasan, *Fuel Cells, From Fundamental and Applications* (Springer US, 2006)
42. H. Okamoto, T. Aso, Japanese Journal of Applied Physics **6**(6), 779 (1967)